Smart Structures and Systems, *Vol. 28, No. 2 (2021) 229-243*
https://doi.org/10.12989/sss.2021.28.2.229

Seismic resistant design of highway bridge with multiple-variable frequency pendulum isolator

Xu Liang [a], Jianian Wen*, Qiang Han [b] and Xiuli Du [c]

Key Laboratory of Urban Security and Disaster Engineering of Ministry of Education, Beijing University of Technology, Beijing, China

(*Received June 16, 2020, Revised May 10, 2021, Accepted May 14, 2021*)

Abstract. Multiple variable frequency pendulum isolator (MVFPI) has been recently developed as a superior alternative to the traditional friction pendulum bearing (FPB) especially for the seismic isolation in near-fault regions. The MVFPI is characterized by its variable frequency and self-adaptability, which are achieved by piecewise function of sliding surface and shape memory alloy (SMA). The objective of this study is to propose the design algorithm of the MVFPIs in highway bridge as an extension of the direct displacement-based design (DDBD) framework. The nonlinearities of the structural components are taken into account in the design procedure, and the corresponding damage states satisfy the two-stage design philosophy. The accuracy and robustness of the design procedure are verified by an isolated four-span highway bridge through nonlinear time history (NLTH) analyses. The analytical results indicate that the proposed design procedure can predict the profile of deck displacement and amplitude, as well as the damage states of the piers. From statistic aspect, the fragility analyses illustrate that the bridge isolated by MVFPIs exhibits better seismic performance than that of the bridge isolated by FPBs.

Keywords: direct-displacement based design; fragility analysis; multiple variable frequency pendulum isolator; nonlinear time history analyses; shape memory alloy

1. Introduction

The seismic vulnerability of highway bridges located in seismically region is of great concern to the researchers and engineers. The seismic isolation strategy has been proven as an effective and economic method in reducing seismic responses. The commonly used seismic isolation devices can be divided by two categories, namely rubber bearing (i.e., lead rubber bearing, laminated rubber bearing, and high damping rubber bearing) and sliding friction bearing (i.e., friction pendulum bearing, double concave sliding bearing, and triple friction pendulum bearing) (Wen *et al*. 2019). The friction pendulum bearing (FPB) offers desired horizontal flexibility, energy dissipation capacity and durability (Han *et al*. 2015), making it well suited for application to highway bridges. However, the traditional FPB inevitably introduce a constant predominant period, which may incur resonance-like behavior in the isolated bridge (Pranesh and Sinha 2000) when subjected to near-fault ground motions containing long-period components. Motivated by the need of solving the resonance problem, a novel multiple-variable frequency pendulum isolator (MVFPI) (Han *et al*. 2020) was proposed, in which the mathematic formulation of sliding surface is a piecewise function. The natural frequency of the MVFPI isolated bridge could be shifted away from the predominant frequency of ground motion. The shape memory alloy (SMA) wires are introduced in MVFPI to restrict the deformation and improve the seismic resilience, due to the excellent energy dissipation and self-centering capacities of SMA. The mechanical properties of the MVFPI have been investigated by a series of quasi-static tests and parametric studies (Han *et al*. 2020). The testing and numerical results demonstrated that the dynamic responses of the MVFPI isolated structure could be controlled within the desired ranges, but a simplified design procedure is needed for the engineering practice.

The performance-based seismic design (PBSD) (Ghobarah 2001) framework proposed by pacific earthquake engineering research (PEER) center connects the seismic performance with the design parameters. The displacement (i.e., drift ratio, material strain, and plastic hinge rotation) (Blandon and Priestley 2005) is an effective damage index to qualify the seismic performance of the structures. Consequently, a direct displacement-based design (DDBD) framework was proposed by Priestley *et al*. (2007) under the concept of PBSD. In recent decades, the DDBD procedure has been extended to various structural types, including the reinforced concrete (RC) and steel frames (Moehle 1992, Pettinga and Priestley 2005, Macedo and Castro 2012, O'Reilly and Sullivan 2016), the shear wall structures (Debnath and Choudhury 2017, Zeris *et al*. 2020), different types of bridges (Kowalsky 2002, Dwairi and Kowalsky 2006, Khan 2015, Han *et al*. 2018), and the structures with soil-foundation-structure interaction (Paolucci *et al*. 2013). With the development and application of seismic isolation, the DDBD procedure has also been adapted for the isolated bridges. Jara and Casas

*Corresponding author, Postdoctoral Researcher,
E-mail: wjn@emails.bjut.edu.cn
[a] Ph.D. Candidate, E-mail: liangxu11@emails.bjut.edu.cn
[b] Professor, E-mail: qhan@bjut.edu.cn
[c] Professor, E-mail: duxiuli@bjut.edu.cn

ISSN: 1738-1584 (Print), 1738-1991 (Online)

(2006) presented an extended DDBD approach for the bridges supported on the lead rubber bearings based upon a derived equivalent damping ratio, and the proposed method improves the displacement prediction capacity. Cardone *et al*. (2009) proposed the DDBD procedure for both existing and new bridges equipped with various types of seismic isolation systems (i.e., rubber bearing and frictional sliding bearing), which were validated by nonlinear time-history (NLTH) analyses on different configurations of the bridges. A new DDBD method for the isolated bridge with viscous dampers was presented by Sanchez and Igarashi (2012), and the proposed method avoids the iterative process. Amiri *et al*. (2016) proposed a DDBD procedure for a continuous girder bridge isolated by triple friction pendulum bearings, and the seismic demands were evaluated by bi-directional near filed ground motions. Li *et al*. (2018) extended the displacement-based seismic design to the restrainers in the isolated bridges based on a linearized 2-degree-of-freedom analytical model to determine the configuration of the restrainers. The DDBD methodology was also utilized in the bridge retrofitted by different braces to achieve the specified seismic performance (Xiang and Alam 2019).

Although previous study demonstrated that the MVFPI is a stable and robust isolation device, the seismic resistant design of highway bridges isolated by MVFPI has not been well investigated. If the MVFPI in bridge is not designed properly, the seismic performance of the overall bridge may degrade. The aforementioned DDBD framework provides a viable option for the seismic design of MVFPI, but traditional DDBD cannot be directly applied. This study aims to develop the seismic resistance design procedure for the highway bridge equipped with MVFPIs as an extension of the aforementioned DDBD procedure. The objectives of the present research are: (1) to propose the seismic design procedure for the highway bridge isolated by MVFPI; (2) to verify the proposed design procedure by NLTH analyses; (3) to investigate the reliability of the isolated bridge with the parameters obtained from DDBD procedure.

2. Design algorithm of MVFPI in highway bridge

2.1 A Brief Introduction of MVFPI

The details of the MVFPI are presented in Fig. 1(a), which is distinguished from FPB by its piecewise function of sliding surface and additional SMA-wires (Han *et al*. 2020). The MVFPI is aimed at mitigating the seismic responses of isolated bridges under different earthquake intensities. The piecewise function is composed of the hyperbolic and exponential functions (as shown in Fig. 1(b)), which conforms with the two-stage design philosophy in Chinese seismic design code (JTJ/T 2008). The hyperbolic function has softening stiffness to reduce the inertia force transferred to the substructure, and the exponential function provides larger stiffness to control the displacement. SMA-wires are also introduced to enhance the seismic resilience at severe earthquake. The piecewise geometric function of MVFPI is given by Han *et al*. (2020)

$$y=\begin{Bmatrix} b\sqrt{1+\dfrac{x^2}{(|x|+d)^2}}-b & x\le x_0 \\ y_0 e^{\frac{y_0'}{y_0}(x-x_0)} & x>x_0 \end{Bmatrix} \tag{1}$$

where b is the imaginary semi-axis; d is the rate of variation of isolator frequency; x_0 is the critical displacement; y_0 and y'_0 are the value and the first derivative of the piecewise function at x_0.

Based on the geometric function in Eq. (1), the lateral force-displacement relationship of the MVFPI can be expressed by (Han *et al*. 2020)

$$\begin{aligned} F&=\begin{Bmatrix} F_r+F_f & |x|\le x_1 \\ F_r+F_f+F_{\mathrm{SMA}} & |x|>x_1 \end{Bmatrix} \\ &=\begin{Bmatrix} mgy'(x)+sgn(\dot{x})\,\mu mg & |x|\le x_1 \\ mgy'(x)+sgn(\dot{x})\,\mu mg+\mathrm{sgn}(x)nA\sigma\cos\theta & |x|>x_1 \end{Bmatrix} \end{aligned} \tag{2}$$

where mg is the gravity force on the bearing; μ is the friction coefficient; A is the area of single SMA-wire; n is the total number of the SMA-wires; σ is the tensile stress in the SMA-wires; x_1 is the displacement when the SMA-wires start in tension (as shown in Fig. 1(c)). The equivalent damping ratio of the MVFPI depends on the geometric function of sliding surface and the mechanical properties of SMA-wires, which is also a piecewise function

$$\xi_{\mathrm{eq}}=\begin{Bmatrix} \dfrac{2}{\pi(\frac{y'}{\mu}+1)} & |x|\le x_1 \\ \dfrac{2\mu mg}{\pi F}+\dfrac{E_{SMA}}{2\pi Fx} & |x|>x_1 \end{Bmatrix} \tag{3}$$

where F is the lateral force of MVFPI in Eq. (1); E_{SMA} is the energy dissipated by SMA-wires.

The equivalent damping ratio of the MVFPI and FPB can be simplified as a function of the dimensionless value Λ, which is obtained as

$$\xi=\frac{2}{\pi(1+\Lambda)} \tag{4}$$

where ξ is the equivalent damping ratio; Λ of MVFPI and FPB can be defined as

$$\begin{aligned} \Lambda_{\mathrm{MVFPI}}&=y'/\mu \\ \Lambda_{\mathrm{FPB}}&=D/\mu R \end{aligned} \tag{5}$$

where D and R are the limited displacement and radius of sliding surface of FPB.

Considering that μ and D/R of FPB are generally ranging from 2% to 5% and 7.5% to 15% (Dolce *et al*. 2005), the equivalent damping ratio is limited between 7.5% and 25%. For MVFPI, the parameter y' is ranging

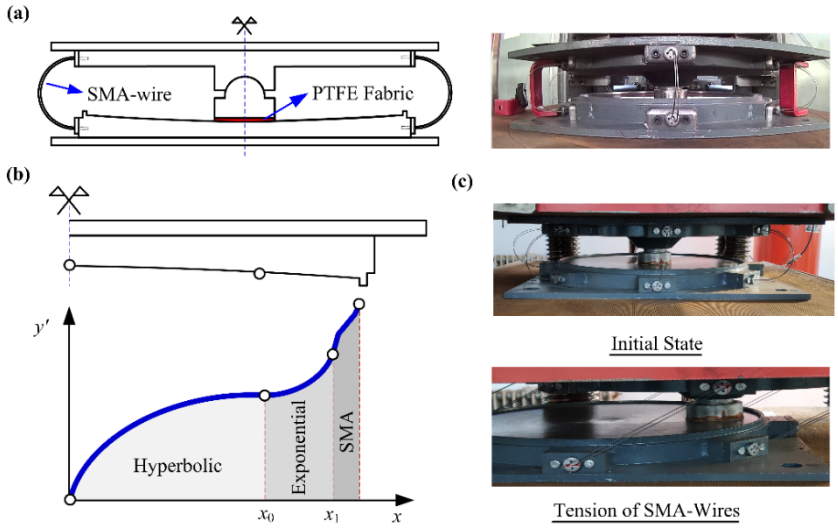

Fig. 1 Fundamentals of MVFPI: (a) configuration; (b) piecewise function of sliding surface; (c) principles of operation. (adapted from Han *et al*. 2020)

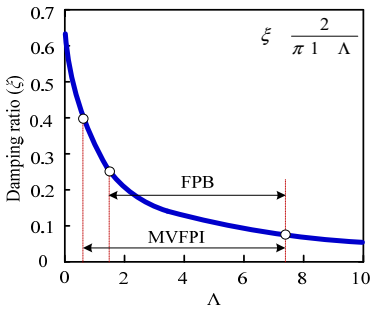

Fig. 2 Equivalent damping ratio of the MVFPI and FPB

from 3% to 15% (Han *et al*. 2020), and the corresponding effective damping ratio varies between 7.5% and 40%, which covers a larger range than FPB. For helping the designer in the selection of the parameters at the beginning of the analysis, the ranges of the equivalent damping ratio of MVFPI and FPB are shown in Fig. 2.

2.2 Design algorithm of MVFPI

The fundamentals of the DDBD algorithm are presented in Fig. 3, using a highway bridge as an example (Priestley 1993). In the design procedure, an equivalent single-degree-

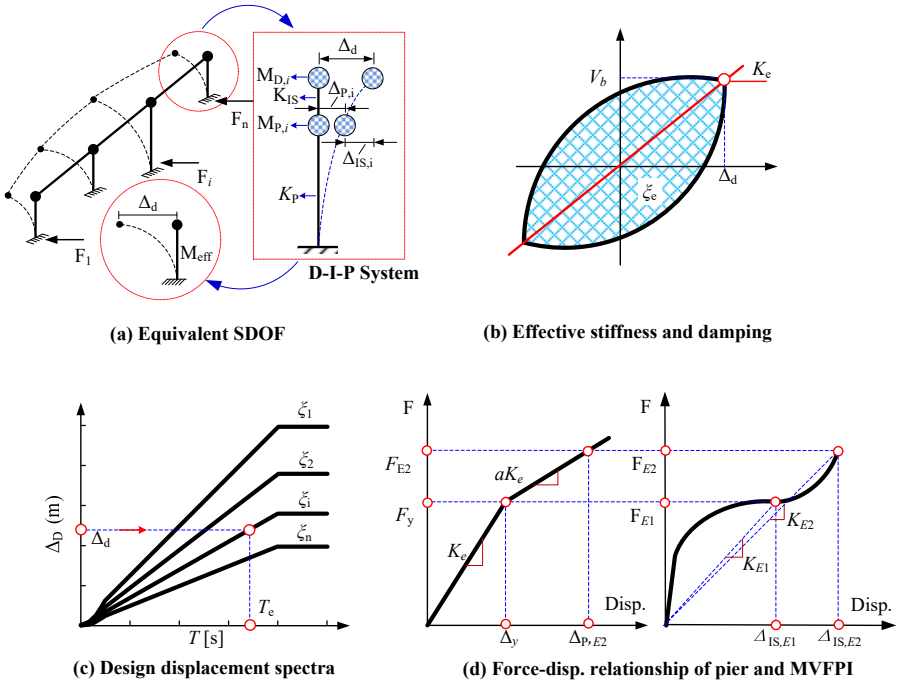

Fig. 3 Fundamentals of DDBD with specific reference to highway bridge

of-freedom (SDOF) (as shown in Fig. 3(a)) is obtained by predefined displacement profile and the displacement capacities of the vulnerable components. The effective stiffness, damping ratio, and mass of the substitute SDOF can be derived (as shown in Fig. 3(b)). Then, the effective period of the equivalent SDOF is determined by the design displacement based on the displacement spectra (as shown in Fig. 3(c)). Finally, the shear force of SDOF can be calculated and equivalently assigned to the original structure.

The above general DDBD procedure is adapted to the design of MVFPIs in the highway bridge. It is worth mentioning that two seismic hazard levels (E1 and E2) are considered in the design procedure of MVFPI. The bridge is required to maintain elastic and intact under E1 earthquake, and only limited damage is allowed under E2 earthquake. Based upon above requirements, the coordinated force-displacement relationships of the pier and MVFPI at different hazard levels are presented in Fig. 3(d). Under E1 seismic intensity level, the piers remain elastic and MVFPI exhibits softening stiffness to reduce the inertia force. Under E2 seismic intensity level, the piers are engaged in the plastic range and the MVFPI is featured by enhanced stiffness to reduce the displacement. The characteristics of the equivalent SDOF are determined by different seismic hazard levels in the following design procedure.

Based on above assumptions, the design procedure of the MVFPI in highway bridges in transverse direction is presented in Fig. 4. In Step 1, the basic input data of the bridge are determined, which includes the design displacement, mass, geometry, reinforcement ratio, etc. The design displacement is the maximum allowable displacement of the bridge, which takes the deformations of the deck, pier, and bearings into account. Based on the appropriate displacement profile of structural components, the original bridge can be simplified into an equivalent SDOF (Priestley *et al*. 2007, Gulkan and Sozen 1974), as shown in Fig. 3(a), and the corresponding design displacement (Δ_d) can be derived by

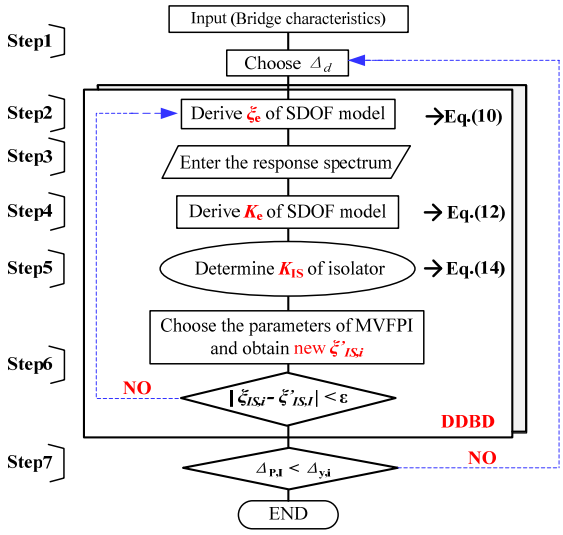

Fig. 4 Flowchart of the DDBD procedure for existing bridge with the MVFPI

$$\Delta_d = \frac{\sum_{i=1}^{n}(m_i \cdot \Delta_i^2)}{\sum_{i=1}^{n}(m_i \cdot \Delta_i)} \tag{6}$$

where i is the number of the piers or abutments; m_i is the equivalent mass at the different locations; and Δ_i is the associated absolute displacement at each m_i. Specifically, the equivalent mass of i-th Deck-Isolator-Pier (D-I-P) system (shown in Fig. 3(a)) in this study is obtained by

$$m_i = \frac{\left(M_{P,i} \cdot \Delta_{P,i} + M_{D,i} \cdot \Delta_{IS,i}\right)^2}{M_{P,i} \cdot \Delta_{P,i}^2 + M_{D,i} \cdot \Delta_{IS,i}^2} \tag{7}$$

where $M_{P,i}$ is the total mass of the pier cap and one third pier; $M_{D,i}$ is the total mass of the half left span and half right span; $\Delta_{P,i}$ and $\Delta_{IS,i}$ are the design displacements of the pier and isolator in the i-th D-I-P system.

In step 2, the equivalent damping ratio of the D-I-P system can be determined by the damping ratios of the MVFPIs and the damping ratios of the piers at the design drift ratio. The equivalent damping ratio of the i-th D-I-P system ($\xi_{eq,i}$) is given by

$$\xi_{eq,i} = \frac{\Delta_{P,i} \cdot \xi_{P,i} + \Delta_{IS,i} \cdot \xi_{IS,i}}{\Delta_{P,i} + \Delta_{IS,i}} \tag{8}$$

where $\xi_{IS,i}$ is the equivalent damping of the isolator at the design displacements; $\xi_{P,i}$ is the equivalent damping of pier, which is a function of displacement ductility (μ) (Kowalsky 2002)

$$\xi_{P,i} = 0.05 + \frac{1 - (1-\alpha)/\sqrt{\mu} - \alpha\sqrt{\mu}}{\pi} \tag{9}$$

where α is the ratio between the post-elastic stiffness and the initial stiffness with a typical value of 0.05.

The equivalent damping (ξ_e) of the SDOF is derived by combining the equivalent damping of each D-I-P system together, which is given by

$$\xi_e = \frac{\sum_{i=1}^{n}\left(F_i \Delta_i \xi_{eq,i}\right)}{\sum_{i=1}^{n}(F_i \Delta_i)} \tag{10}$$

where the F_i is the design strength of each D-I-P system at design displacement (Priestley *et al*. 2007). The damping reduction factor (R_ξ) is required to derive the high damping response spectra, which is expressed by Eurocode 8 (1998)

$$R_\xi = \left(\frac{0.07}{0.02 + \xi_e}\right)^{0.5} \tag{11}$$

In step 3, the design spectrum is then determined for the equivalent SDOF at a specific site with the given equivalent damping. The effective period (T_e) can be directly read from the spectra at a given design displacement (Δ_d).

In step 4, the equivalent stiffness (K_e) of the equivalent SDOF system is determined by

$$K_e = \frac{4\pi^2 \cdot M_e}{T_e^2} \tag{12}$$

where M_e is the equivalent mass of the SDOF, which can be derived based on displacement profile

$$M_e = \frac{\sum_{i=1}^{n}(m_i \cdot \Delta_i)}{\Delta_d} \quad (13)$$

In Step 5, the equivalent stiffness ($K_{IS,i}$) of MVFPI in the i-th D-I-P system can be solved by the following equation

$$\frac{1}{K_{eq,i}} = \frac{1}{K_{P,i}} + \frac{1}{K_{IS,i}} \quad (14)$$

where $K_{P,i}$ is the equivalent stiffness of the pier at the design displacements; the equivalent stiffness ($K_{eq,i}$) of i-th D-I-P system is defined as F_i/Δ_i, in which the F_i is the inertial force in the i-th system

$$F_i = \frac{m_i\Delta_i}{\sum_1^n m_i\Delta_i} V_b \quad (15)$$

where V_b is the base shear of the SDOF, which equals to $K_e\Delta_d$.

In Step 6, based on the derived equivalent stiffness of the MVFPI, the parameters of the isolator in the i-th D-I-P system can be determined and consequently a new equivalent damping ($\xi'_{IS,i}$) of MVFPI is obtained. If the absolute value between the new equivalent damping ratio and predefined damping ratio of MVFPI is more than specified tolerance, the previous steps are repeated to update the equivalent damping of MVFPI until a convergence is reached.

Table 1 Material properties of concrete and steel reinforcement

Material	Property	Value
Concrete	Compression strength (Mpa)	30
	Young's modulus (Mpa)	36000
	Strain at peak stress (%)	0.2
Steel	Yield stress (Mpa)	420
	Young's modulus (Mpa)	200000

Finally, the new design displacements of the piers should be checked to guarantee the appropriate state of the pier. If the pier is yield in the E1 design stage, iterations are still needed to update the design displacement of the pier in Step 1 until it is in the elastic range, and also the displacement of pier at E2 design stage should be less than the design displacement ($\Delta_{P,E2}$).

3. Numerical validation

3.1 Bridge prototype and FE model

The prototype of the highway bridge in this study is adapted from Priestley *et al*. (2007). The continuous girder bridge consists of four spans (40 m + 50 m + 50 m + 40 m), supported on three piers with unequal height of 8 m, 6 m, and 8 m, as shown in Fig. 5(a). The RC deck has a box section of 14 m wide by 2 m deep (shown in Fig. 5(b)), and the weight per unit of length is 190 kN/m. The MVFPIs are placed between the deck and piers (as shown in Fig. 5(b)). The RC piers have uniform circular section of 1.2 m in diameter, and the arrangement of the rebars is presented in Fig. 5(c). The material properties of concrete and steel reinforcement are shown in Table 1.

3.2 Model numerical implement of MVFPI

The three-dimensional (3D) finite element (FE) model of the continuous girder bridge isolated by MVFPI was developed in the OpenSees platform. OpenSees platform is an open source object-oriented framework for finite element analysis using C++ programming language. There are some bearing elements and uniaxial materials in OpenSees library which can be used for describing the force-displacement behavior of FPB and SMA, but these bearing models are not suitable for the MVFPI. A new "singleMVFPI" element was developed in the OpenSees platform, which is defined by two nodes with same coordinates in 3D space (Fenz 2008, Dao *et al*. 2013). The mechanical model of the MVFPI as stated in section 2.1 is extended to a bi-

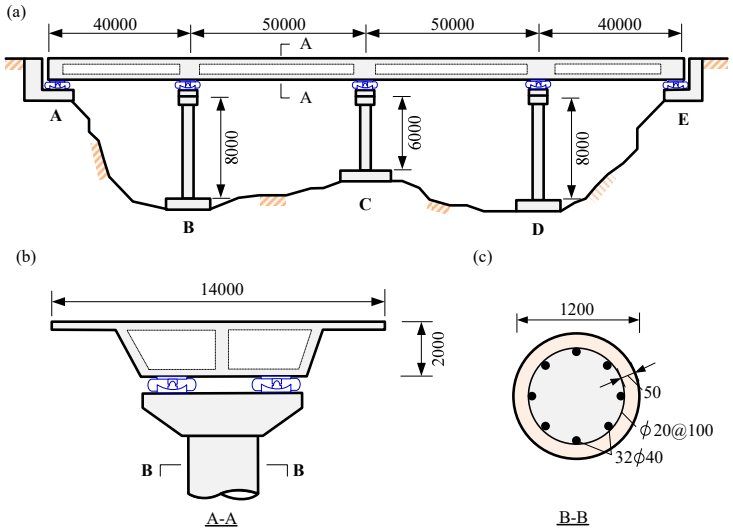

Fig. 5 Prototype of the bridge: (a) bridge configuration; (b) elevation view; and (c) section view of pier. (unit: mm)

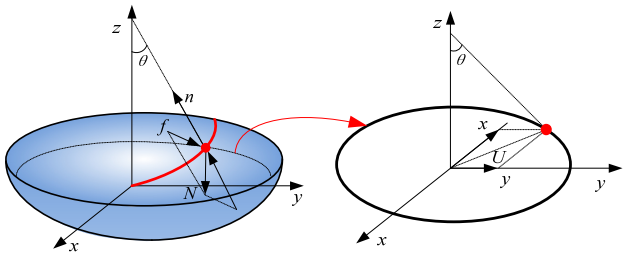

Fig. 6 Force and displacement relationship on the MVFPI in 3D Space

directional model. As shown in Fig. 6, the horizontal displacement of the MVFPI is composed of x and y directions, which can be expressed as

$$U = \sqrt{x^2 + y^2} \tag{16}$$

where x and y are the sliding displacements in two orthogonal directions.

Substituting Eq. (16) into Eq. (1), the geometric function of the sliding surface can be expressed as

$$Y = \begin{cases} b\sqrt{1 + \dfrac{U^2}{(|U| + d)^2}} - b & U \le U_0 \\ Y_0 e^{\frac{U_0'}{Y_0}(U - U_0)} & U > U_0 \end{cases} \tag{17}$$

where U is the horizontal displacement of the MVFPI; Y is the vertical displacement of the slider. The bi-directional force-displacement relationship of the bearing can be derived as Mosqueda *et al*. (2004)

$$\begin{Bmatrix} f_x \\ f_y \end{Bmatrix} = N \begin{bmatrix} \dfrac{\partial Y}{\partial x} & 0 \\ 0 & \dfrac{\partial Y}{\partial y} \end{bmatrix} \begin{Bmatrix} dx \\ dy \end{Bmatrix} + \mu N \frac{1}{\|\dot{U}\|} \begin{Bmatrix} \dot{x} \\ \dot{y} \end{Bmatrix} \tag{18}$$

where f_x and f_y are the forces in two orthogonal directions; $\partial Y/\partial x$ and $\partial Y/\partial y$ are the partial derivatives of geometric function Y in two orthogonal directions; N is the vertical load, $\|\dot{U}\|$ is the norm of horizontal velocity; $\dot{x}$ and $\dot{y}$ are the sliding speed of the bearing in two orthogonal directions. The bi-directional plasticity model with circular yield surface proposed by Simo and Hughes (1998) was implemented to develop the "singleMVFPI" element in a normalized domain with normalized force and stiffness.

The numerical model of MVFPI consists of a "singleMVFPI" element and a zero-length element of SMA-wires in parallel. The SMA-wires are simulated by Self-Centering and Gap material in parallel. In order to verify the accuracy of the proposed numerical model, the pushover analysis was performed on the MVFPI model in OpenSees and compared with the test results (Han *et al*. 2020). The design parameters are listed in Table 2. Fig. 7 presents the comparison of MVFPI force-displacement between numerical and experimental results. It can be found that the MVFPI force-displacement loops of the numerical

Table 2 The design parameters of MVFPI

Parameter	b (m)	d (m)	x_0 (m)	x_1 (m)	x_2 (m)	T_0 (s)
Value	0.16	0.30	0.10	0.13	0.15	1.50

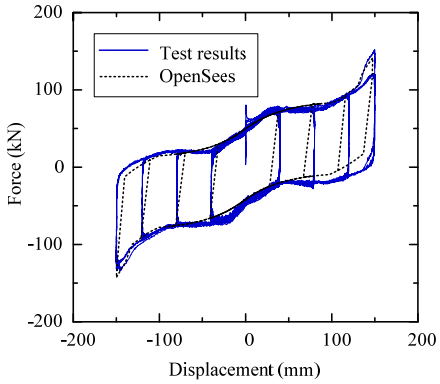

Fig. 7 Comparison of MVFPI force-displacement between numerical and experimental results

analysis agree well with those of test results. The MVFPI element developed in OpenSees is accurate enough for the further practical application in the numerical analysis.

3.2 FE model of the isolated continuous girder bridge

The three-dimensional (3D) finite element (FE) model of the continuous girder bridge isolated by MVFPI is shown in Fig. 8. The deck is modeled by elastic beam-column elements. The values of Young's modulus and Poisson's ratio for the RC deck are taken as 36000 MPa and 0.2, respectively. The moment of inertia in transverse direction and area of the deck are 87 m^4 and 6.88 m^2. The MVFPI is consists of "singleMVFPI" element and a zero-length element of SMA in parallel (shown in Fig. 8). The stress-strain relationship of SMA is shown in Fig. 8. The piers are simulated by 3D displacement-based beam-column elements with fiber sections. The section of pier is discretized into confined fibers, unconfined fibers, and rebars. The confined and unconfined concrete is described by Kent-Scott-Park material (Concrete01 in OpenSees). The parameters of the constitutive model are presented in Table 3. The rebars are simulated by Giuffré-Menegotto-Pinto model, namely Steel02 in OpenSees. The Young's modulus, yield stress, and hardening ratio are 2×10^5 MPa, 420 Mpa, and 0.01. The yield displacements of the pier B ($\Delta_{y,B}$),

Table 3 Parameters for Kent-Scott-Park concrete material model

Concrete material parameters in OpenSees	Confined concrete	Unconfined concrete
Compressive strength, fpc (Mpa)	39	30
Strain at maximum stress, epsc0 (1)	0.0026	0.002
Ultimate stress, fpcu (MPa)	7.8	6
Strain at ultimate stress, epsU (1)	0.0143	0.004

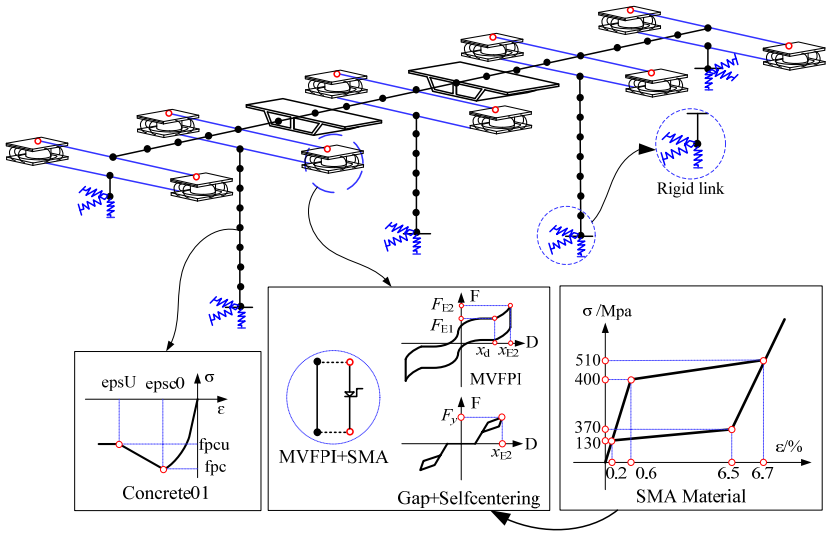

Fig. 8 3D finite element model of the continuous girder bridge

C ($\Delta_{y,C}$), and D ($\Delta_{y,D}$) are 0.102 m, 0.059 m, and 0.102 m. The soil-pile interaction in the bridge is neglected, because the bridge is supported on the bedrock.

3.2 Verification study

A series of NLTH analyses were conducted on the four-span continuous girder bridge in transverse direction to verify the proposed design procedure. Seven ground motions were artificially generated to match the design response spectrum, and then the PGAs of the ground motions were scaled to E1 and E2 hazard levels. The hazard levels of E1 and E2 (corresponding to 10% and 2% in 50 years return period) have PGAs of 0.4 g and 0.6 g at the bridge site. The generated ground motion records and the corresponding individual and average displacement spectrum are presented in Fig. 9.

The detailed design process of the MVFPIs in the continuous girder bridge along transverse direction is presented in Appendix I, and the final design parameters of MVFPI are listed in Table 4.

Fig. 10 presents the comparison between the design displacements, the peak displacements obtained from NLTH analyses, and the corresponding average peak displacement of the MVFPIs. It can be found that the proposed displacement profiles agree well with these from NLTH analyses under both E1 and E2 hazard levels. The design objectives and NLTH results are compared in Table 5, in which $D_{D,MVFPI}$ and $D_{D,\ pier}$ denote the design displacement of the MVFPI and piers; $D_{NL,MVFPI}$ and $D_{NL,MVFPI}$ denote the

Table 4 Final design parameters of MVFPI

Parameter	Abutment A & E	Pier B & D	Pier C
b (m)	0.367	0.396	0.376
d (m)	0.604	0.627	0.611
Initial period (s)	2.000	2.000	2.000
Design displacement at E1 level (m)	0.250	0.199	0.220
Design displacement at E2 level (m)	0.375	0.253	0.304
Friction coefficient (1)	0.050	0.050	0.050
SMA wires area (m^2)	2.367×10^{-4}	8.962×10^{-4}	8.121×10^{-4}

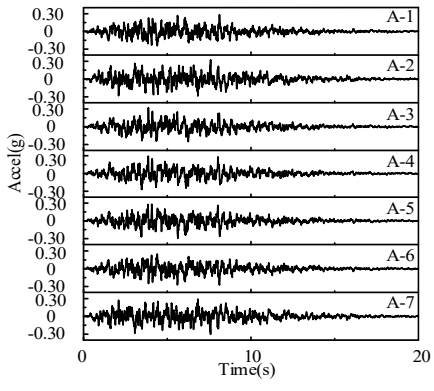

(a) Acceleration time history

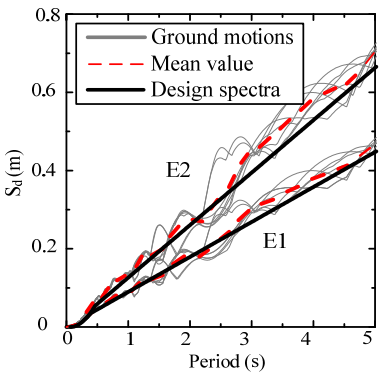

(b) Displacement spectrum

Fig. 9 The artificial ground motions used in the NLTH analysis

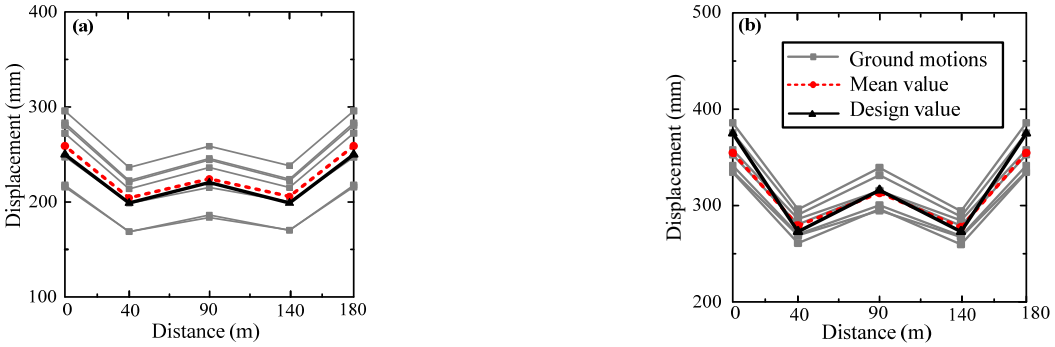

(a) E1 (b) E2

Fig. 10 Comparison of peak displacement of MVFPI at E1 and E2 hazard levels

Table 5 Comparison between the design objectives and NLTH results

Level	Location	$D_{D,MVFPI}$ (mm)	Mean $D_{NL,MVFPI}$ (mm)	$D_{D,pier}$ (mm)	Mean $D_{NL,pier}$ (mm)	Error of D_{MVFPI}	Error of D_{pier}
E1	A&E	250.00	249.10	-	-	0.01	-
	B&D	199.00	195.10	51	60.2	-0.02	0.18
	C	220.00	214.28	30	35.8	-0.03	0.19
E2	A&E	375.00	358.22	-	-	-0.04	-
	B&D	258.00	262.33	122	100.9	-0.04	-0.10
	C	304.00	301.45	70.8	67.0	-0.05	0.05

(a) E1 (b) E2

Fig. 11 Hysteresis curves of MVFPI at different intensity levels

displacement of the MVFPI and piers obtained from NLTH analyses. It can be seen that the discrepancies of the peak displacement are less than 5%, and the errors in terms of the displacements at the top of the piers are in the range of 1-19%.The reasons of the discrepancies between NLTH analyses and proposed design procedure can be contributed to: (1) in the design procure, it is assumed that the fundamental mode dominates the seismic response in the highway bridge without considering the contribution of the higher modes; (2) the damping reduction factor is needed to modify the elastic design spectra when an equivalent linearization approach is used in the design procedure, which is not accurate enough to account for the energy dissipation capacity of the bridge (Calvi 2019).

Fig. 11 presents the hysteretic curves of the MVFPI at the abutment when subjected to A-1 ground motion. As expected, the stiffness is softened with the increasing of the displacement under E1 level, as shown in Fig. 11(a). When the displacement of MVFPI exceeds the design displacement under E1 level, the enhanced stiffness can be observed. Simultaneously, SMA-wires could provide additional restoring force to improve the seismic resilient at the E2 intensity level (as shown in Fig. 11(b)).

4. Fragility analysis of isolated highway bridge

4.1 Fragility methodology

Fragility analysis could assess the damage probability of the isolated bridge with the parameters obtained from the DDBD design procedure (Dezfuli and Alam 2016). In this section, the fragility analyses are conducted to evaluate the relative vulnerability of the bridge isolated by MVFPIs and FPBs. The probabilistic seismic demand model (PSDM) is employed in this study to derive the fragility functions of the fragile components (i.e., piers and isolators) and bridge system. The fragility function can be defined as the

conditional probability of the seismic demand (D) exceeding the structural capacity (C) at a certain intensity measure (IM), which is expressed by

$$P[D \geq C|IM] = \Phi\left[\frac{ln(\mu_D/S_c)}{\sqrt{\beta_{D|IM}^2 + \beta_c^2}}\right] \quad (19)$$

where Φ is the standard normal cumulative distribution function; μ_D is the median estimate of the demand; S_c is the median estimation of the capacity; β_c and $\beta_{D|IM}$ are the logarithmic standard deviation of the capacity and the seismic demand conditioned on the IM (Amirihormozaki 2013). The parameters can be estimated by a linear regression analysis in the log-transformed space

$$ln(\mu_D) = ln(a) + b\, ln(\mathrm{IM}) \quad (20)$$

$$\beta_{D|IM} = \sqrt{\frac{\sum_{i=1}^{N}\left[\ln(EDP_i) - \left(\ln(a) + bln(IM_i)\right)\right]^2}{N-2}} \quad (21)$$

where a and b are the regression coefficients; EDP_i is the i^{th} seismic demand from the simulation; N is the total number of simulations.

In order to investigate the seismic performance of the pier-isolation system, the system-level fragility functions are developed. The isolator and pier at different locations can be considered as a serial system (I-P system), the lower and upper bound of the system-level fragility function (p_{sys}) can be obtained by following equation

$$\max_{i=1}^{n} p_i \leq p_{sys} \leq 1 - \prod_{i=1}^{n}[1 - p_i] \quad (22)$$

where p_i is the probability of failure of the i-th component. As recommended by previous study (Choi *et al*. 2004), the conservative upper bound would be a more appropriate selection.

Four different damage states recommended by HAZUS (2003) are considered in this study, i.e., slight, moderate, extensive, and collapse. The damage states of the piers are quantified by the displacement ductility, which are listed in Table 6. It should be noted that there is no available data regarding the damage states of the friction sliding bearings. Therefore, when the bearing reaches or exceeds the limit displacements, this state is defined as slight damage (Shi 2018).

The highway bridge used for the fragility analysis has been shown in Fig. 5. The final design parameters of MVFPI are listed in Table 4. For comparison purpose, the fragility functions of the bridge isolated by FPBs are also presented here. The same procedure as described in section 2.2 is employed to obtain the parameters of the FPBs. The equivalent radii are 1.6 m (A and E), 1.1 m (B and D), 1.3 m (C); the design displacements are 0.375 m (A and E), 0.253 m (B and D), 0.304 m (C); and the friction coefficient of the FPBs is 0.05.

Table 6 Damage states of the pier (Huo and Zhang 2013)

Component	Damage index	Damage states			
		Slight	Moderate	Extensive	Collapse
Pier	Displacement ductility	$\mu > 1.00$	$\mu > 1.20$	$\mu > 1.76$	$\mu > 4.76$

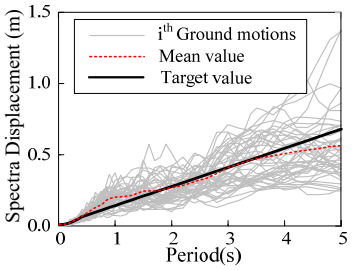

Fig. 12 Displacement spectra of ground motion records

In order to consider the uncertainties and randomness of ground motions to develop the fragility functions, 65 ground motion records are selected from PEER database (PEER 2013), which are listed in Appendix II. For the selected ground motion records, the PGAs vary from 0.2 to 0.9 g. The spectra of the selected ground motions, the corresponding average spectrum, and the target spectrum used in the DDBD are shown in Fig. 12. It is obvious that the average spectrum agrees well with the target spectrum. The ground motions can be characterized by different IMs (i.e., PGA, spectral acceleration at the fundamental period (Sa,T_1), PGV (peak ground velocity), and Arias Intensity (AI)). Previous studies have demonstrated that PGA is an efficient and practical IM for relating to the EDPs, therefore, the PGA is selected as the IM for conducting the seismic fragility analysis.

4.2 Fragility analysis

Fig. 13 presents the PSDMs of the peak displacement of different bearings. In order to generate the PSDMs, the selected ground motions are used to perform the NLTH analyses, from which the peak displacements are obtained and plotted against the PGAs in the logarithmic space. The linear regressions are carried out to obtain a and b in Eq. (20), which are listed in Fig. 13. According to the regression coefficients and standard deviations of the seismic demand, the fragility curves of the isolator can be derived based on Eq. (19). Fig. 14 shows the comparison of the fragility curves of MVFPI and FPB at different locations. In all cases, the MVFPI has slightly smaller damage potential compared with that of FPB in entire IMs. Quantitatively, the damage probabilities of the MVFPI and FPB at abutments are 18% and 22% under E2 intensity level (0.6 g), and 5% and 8% under E1 intensity level (0.4 g). The reason is that the stiffness of MVFPI is enhanced by the exponential function to limit the displacement, and also the SMA-wires could provide additional restoring force and energy dissipation.

Fig. 15 shows the computed displacement ductility against the corresponding PGAs in logarithmic scale. Based on Eq. (20), the constants can be obtained by the simulation results, which are presented in Fig. 15. It can be observed

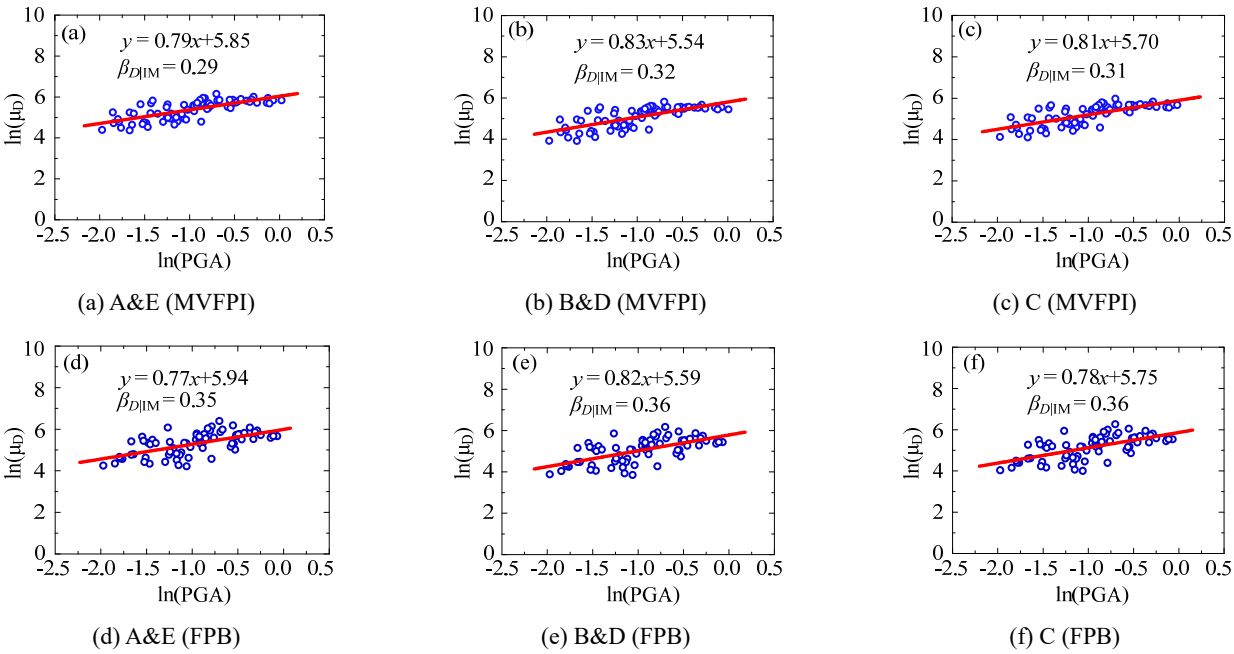

(a) A&E (MVFPI) (b) B&D (MVFPI) (c) C (MVFPI)

(d) A&E (FPB) (e) B&D (FPB) (f) C (FPB)

Fig. 13 The PSDMs for the peak displacements of at different locations

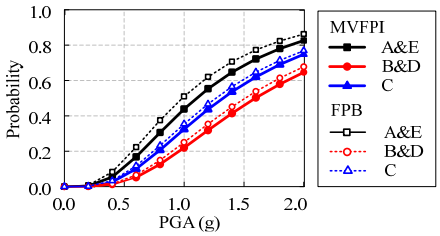

Fig. 14 Fragility curves of MVFPI and FPB

that the intercepts and slopes of the pier B and D are larger than those of the pier C, the pier B and D are more flexible. Fig. 16 presents the fragility curves of the piers isolated by MVFPIs and FPBs at different locations. Obviously, the piers in the bridge isolated by MVFPIs have smaller damage potential compared with that of piers in the bridge isolated by FPBs, and the damage probabilities of the pier B and D in the bridge isolated by MVFPIs reduce by 5% and 12% at E1 and E2 levels. The damage probabilities of the pier C are 15% and 28% at E1 and E2 levels, which is larger than the other piers.

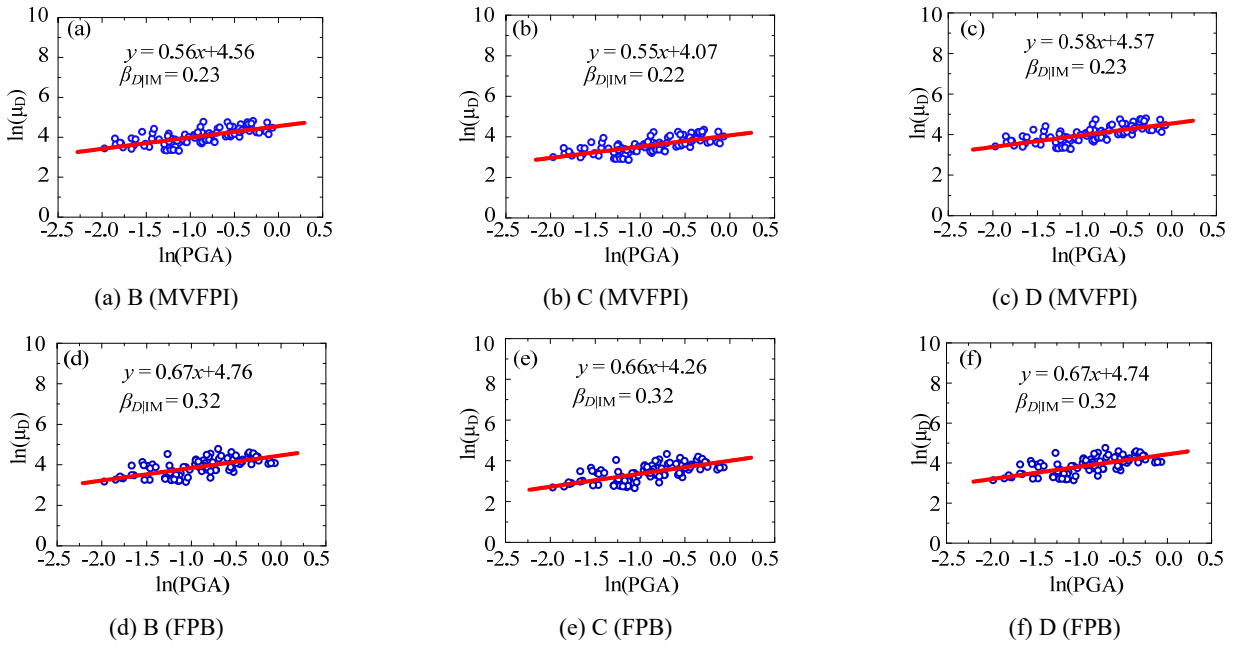

(a) B (MVFPI) (b) C (MVFPI) (c) D (MVFPI)

(d) B (FPB) (e) C (FPB) (f) D (FPB)

Fig. 15 The PSDMs for the piers at different locations

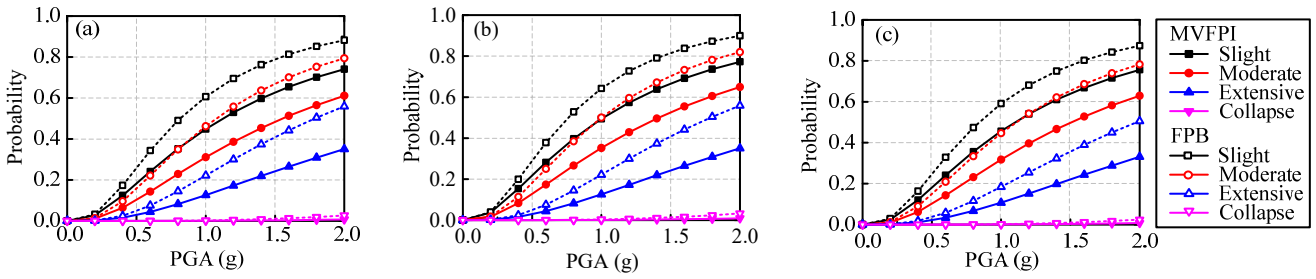

(a) B (b) C (c) D

Fig. 16 Fragility curves for the piers isolated by MVFPI and FPB

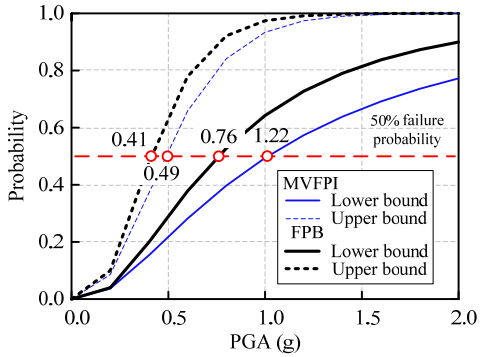

Fig. 17 I-P system fragility curves with MVFPI and FPB

Fig. 17 presents the fragility curves of the I-P systems according the Eq. (22). It is demonstrated that the MVFPI isolated bridge has smaller damage probability compared with FPB isolated bridge. The median PGAs of the system fragility function are listed in Fig. 17. The median value represents the PGA required to achieve 50% damage probability (Huo and Zhang 2013). The larger IMs indicate smaller failure probability. One can conclude from Fig. 17 that the MVFPI outperforms the FPB in the seismic control of highway bridge.

5. Conclusions

In this study, the DDBD procedure was developed for the highway bridge isolated by MVFPIs in its transverse direction. In the design procedure, an equivalent SDOF of the bridge was obtained based on the predefined displacement profile, and two seismic hazard levels (E1 and E2) are considered in the procedure. The proposed design algorithm was applied to a four-span highway bridge equipped with MVFPIs. A 3D FE model of the bridge including the new MVFPI element was built in the OpenSees. The NLTH analyses were conducted on the FE model to verify the proposed design process. Based on the design parameters obtained from the design procedure, the damage probability of the bridge with MVFPIs was compared with the bridge isolated by FPBs. The following conclusions can be drawn from this study:

- The accuracy of the new MVFPI element developed in OpenSees platform was validated by the pseudo-static test. It is indicated that the proposed MVFPI element is accurate enough for the implementation in the NLTH analysis.
- The NLTH analyses results of the isolated highway bridge illustrate that the proposed procedure in general provides the accurate results in terms of the displacement profiles and amplitudes. Moreover, the damage states of the piers remain within the specified limit states.
- The fragility analyses of the isolated bridge demonstrate that the damage probabilities of the bridge isolated by MVFPIs are smaller than those of FPBs, which indicates the better performance of MVFPIs in the seismic control of highway bridge.
- Generally, the seismic performance of MVFPI is superior than traditional FPB, and the design procedure for the highway bridge with MVFPIs can be easily implemented in engineering practice.

Acknowledgments

This research is jointly funded by the National Key of Research and Development of China (2018YFC1504306), National Natural Science Foundation of China (NSFC) (Grants No. 51421005, 51838010) and Beijing Municipal Education Commission (IDHT20190504). These supports are gratefully acknowledged. The results and conclusions presented in the paper are those of the authors and do not necessarily reflect the view of the sponsors.

References

Amiri, G.G. Shalmaee, M.M. and Namiranian, P. (2016), "Evaluation of a DDB design method for bridges isolated with triple pendulum bearings", *Struct. Eng. Mech., Int. J.*, **59**(5), 803-820. https://doi.org/10.12989/sem.2016.59.5.803

Amirihormozaki, E. (2013), "Analytical Fragility Functions for Horizontally Curved Steel Girder Highway Bridges", *Proceedings of the 7th National Seismic Conference on Bridges and Highways*.

Blandon, C.A. and Priestley, M.J.N. (2005), "Equivalent viscous damping equations for direct displacement based design", *J. Earthq. Eng.*, **9**(2), 257-278. https://doi.org/10.1142/S1363246905002390

Calvi, G.M. (2019), "On the correction of spectra by a displacement reduction factor in direct displacement-based seismic design and assessment", *Earthq. Eng. Struct. D*, **48**(6), 678-685. https://doi.org/10.1002/eqe.3159

Priestley, M.J.N., Calvi, G.M. and Kowalsky, M.J. (2007),

"Displacement-based seismic design of structures", New Zealand Conference on Earthquake Engineering, IUSS Press.
Cardone, D., Dolce, M. and Palermo, G. (2009), "Direct displacement-based design of seismically isolated bridges", *B. Earthq. Eng.*, **7**(2), 391. https://doi:10.1007/s10518-008-9069-2
Choi, E., DesRoches, R. and Nielson, B. (2004), "Seismic fragility of typical bridges in moderate seismic zones", *Eng. Struct.*, **26**(2), 187-199. https://doi.org/10.1016/j.engstruct.2003.09.006
Dao, N.D., Ryan, K.L., Sato, E. and Tomohiro, S (2013), "Predicting the displacement of triple pendulum™ bearings in a full-scale shaking experiment using a three-dimensional element", *Earthq. Eng. Struct. D*, **42**(11), 1677-1695. https://doi.org/10.1002/eqe.2293
Debnath, P.P. and Choudhury, S. (2017), "Nonlinear analysis of shear wall in unified performance based seismic design of buildings", *Asian J. Civil Eng.*, **18**(4), 633-642.
Dezfuli, F.H. and Alam, M.S. (2016), "Seismic vulnerability assessment of a steel-girder highway bridge equipped with different SMA wire-based smart elastomeric isolators", *Smart Mater. Struct.*, **25**(7), 075039. https://doi.org/10.1088/0964-1726/25/7/075039
Dolce, M., Cardone, D. and Croatto, F. (2005), "Frictional behavior of steel-PTFE interfaces for seismic isolation", *B. Earthq. Eng.*, **3**(1), 75-99. https://doi:10.1007/s10518-005-0187-9
Dwairi, H. and Kowalsky, M. (2006), "Implementation of Inelastic Displacement Patterns in Direct Displacement-Based Design of Continuous Bridge Structures", *Earthq. Spectra*, **22**(3), 631-662. https://doi.org/10.1193/1.2220577
Eurocode 8. (1998), Design of Structures for Earthquake Resistance, Part 1: General rules seismic actions and rules for buildings, European Committee for Standardization; Brussels Belgium.
FEMA Hazus-MH MR4 (2003), Multi-hazard loss estimation methodology: earthquake model, Federal Emergency Management Agency; Washington DC, USA.
Fenz, D.M. (2008), "Development implementation and verification of dynamic analysis models for multi-spherical sliding bearings", State University of New York Buffalo, USA.
Ghobarah, A. (2001), "Performance-based design in earthquake engineering: state of development", *Eng. Struct.*, **23**(8), 878-884. https://doi.org/10.1016/S0141-0296(01)00036-0
Gulkan, P. and Sozen, M.A. (1974), "Inelastic responses of reinforced concrete structures to earthquake motions", *J. Am. Concrete Inst.*, **71**(12), 604-610.
Han, Q. Wen, J. and Du, X. (2015), "Nonlinear response of continuous girder bridges with isolation bearings under bi-directional ground motions", *J. Vibroeng.*, **17**(2), 816-826.
Han, Q., Wen, J., Du, X., Zhong, Z. and Hao, H. (2018), "Simplified seismic resistant design of base isolated single pylon cable-stayed bridge", *B. Earthq. Eng.*, **16**(10), 5041-5059. https://doi.org/10.1007/s10518-018-0382-0
Han, Q., Liang, X., Wen, J., Zhang, J., Du, X. and Wang, Z. (2020), "Multiple-variable frequency pendulum isolator with high-performance materials", *Smart Mater. Struct.*, **29**(7), 075002. https://doi:10.1088/1361-665x/ab8749
Huo, Y. and Zhang, J. (2013), "Effects of Pounding and Skewness on Seismic Responses of Typical Multispan Highway Bridges Using the Fragility Function Method", *J. Bridge Eng.*, **18**(6), 499-515. https://doi:10.1061/(asce)be.1943-5592.0000414
Jara, M. and Casas, J.R. (2006), "A direct displacement-based method for the seismic design of bridges on bi-linear isolation devices", *Eng. Struct.*, **28**(6), 869-879. https://doi.org/10.1016/j.engstruct.2005.10.016
JTJ/T B02-01-2008 (2008), Guidelines for Seismic Design of Highway Bridges, CMCT, ChongQing China. [In Chinese]
Khan, E. (2015), "Direct displacement based seismic design of continuous curved bridges", Ph.D. Dissertation; North Carolina State University, NC, USA.
Kowalsky, M.J. (2002), "A displacement-based approach for the seismic design of continuous concrete bridges", *Earthq. Eng. Struct. D*, **31**(3), 719-747. https://doi.org/10.1002/eqe.150
Li, S., Dezfuli, F.H., Wang, J.Q. and Alam M.S. (2018), "Displacement-based seismic design of steel FRP and SMA cable restrainers for isolated simply supported bridges", *J. Bridge Eng.*, **23**(6), 4018032. https://doi.org/10.1061/(asce)be.1943-5592.0001231
Macedo, L. and Castro, J.M. (2012), "Direct displacement-based seismic design of steel moment frames", *Proceedings of 15th World Conference on Earthquake Engineering*, Lisbon, Portugal.
Moehle, J.P. (1992), "Displacement-based design of RC structures subjected to earthquakes", *Earthq. Spectra*, **8**(3), 403-428. https://doi.org/10.1193/1.1585688
Mosqueda, G., Whittaker, A.S. and Fenves, G.L. (2004), "Characterization and modeling of friction pendulum bearings subjected to multiple components of excitation", *J. Struct. Eng.*, **130**(3), 433-442. https://doi:10.1061/(asce)0733-9445(2004)130:3(433)
O'Reilly, G.J. and Sullivan, T.J. (2016), "Direct displacement-based seismic design of eccentrically braced steel frames", *J. Earthq. Eng.*, **20**(2), 243-278. https://doi.org/10.1080/13632469.2015.1061465
Paolucci, R., Figini, R. and Petrini, L. (2013), "Introducing dynamic nonlinear soil-foundation-structure interaction effects in displacement-based seismic design", *Earthq. Spectra*, **29**(2), 475-496. https://doi:10.1193/1.4000135
PEER (Pacific Earthquake Engineering Research) (2013), NGA database. https://ngawest2.berkeley.edu
Pettinga, J.D. and Priestley, M.J.N. (2005), "Dynamic behaviour of reinforced concrete frames designed with direct displacement-based design", *J. Earthq. Eng.*, **9**(SI2), 309-330. https://doi:10.1142/s1363246905002419
Pranesh, M. and Sinha, R. (2000), "VFPI: an isolation device for aseismic design", *Earthq. Eng. Struct. D*, **29**(5), 603-627. https://doi.org/10.1002/(SICI)1096-9845(200005)29:5<603::AID-EQE927>3.0.CO;2-W
Priestley, M.J.N. (1993), "Myths and fallacies in earthquake engineering-conflicts between design and reality", *Bull. New Zealand Nat. Soc. Earthq. Eng.*, **26**(3), 329-341.
Sanchez-Flores, F. and Igarashi, A. (2012), "Displacement-based seismic design of base-isolated with bridges with viscous dampers", *Proceedings of the 15th World Conference on Earthquake Engineering*, Lisbon, Portugal.
Shi, Y. (2018), "Seismic Fragility Analysis of FPS isolated High-speed Railway Bridge Based on Response Surface Method", Ph.D. Dissertation; Guangzhou University, GuangZhou, China. [In Chinese]
Simo, J. and Hughes, T. (1998), *Computational Inelasticity*, New York: Springer, NY, USA.
Wen, J., Han, Q. and Du, X. (2019), "Shaking table tests of bridge model with friction sliding bearings under bi-directional earthquake excitations", *Struct. Infrastruct. E.*, **15**(9), 1264-1278. https://doi:10.1080/15732479.2019.1618350
Xiang, N. and Alam, M.S. (2019), "Displacement-based seismic design of bridge bents retrofitted with various bracing devices and their seismic fragility assessment under near-fault and far-field ground motions", *Soil Dyn. Earthq. Eng.*, **119**, 75-90. https://doi:10.1016/j.soildyn.2018.12.023
Zeris, C. Lalas, A. and Spacone, E. (2020), "Performance of torsionally eccentric RC wall frame buildings designed to DDBD under bi-directional seismic excitation", B. Earthq. Eng., **18**(7), 3137-3165. https:// doi:10.1007/s10518-020-00813-3.

BS

Appendix I

Table I Design process of MVFPIs in the bridge

		Abutment A & E	Pier B & D	Pier C
Step1	Design displacement	$\Delta_A = 0.34\ m$	$\Delta_B = 0.24\ m$	$\Delta_C = 0.18\ m$
	Mass	$m_A = 387.75\ t$	$m_B = 892.53\ t$	$m_C = 984.44\ t$
	Equivalent displacement of SDOF	E1 hazard level: $\Delta_{\mathrm{d,E1}} = 0.25\ m$ E2 hazard level: $\Delta_{\mathrm{d,E2}} = 1.5\ \ \Delta_{\mathrm{d,E1}} = 0.375\ m$		
	Equivalent mass	$m_e = 3320\ t$		
Step2	Isolator displacement (E1)	$\Delta_A = 250$ mm	$\Delta_B = \Delta_{\mathrm{E1}} - 0.5\Delta_{y,B}$ $= 199$ mm	$\Delta_C = \Delta_{\mathrm{E1}} - 0.5\Delta_{y,C}$ $= 220$ mm
	Displacement ductility u	-	1.2	1.2
	Isolator Displacement (E2)	$\Delta_{\mathrm{A,E2}} = 375$ mm	$\Delta_{\mathrm{B,E2}} = \Delta_{\mathrm{E2}} - u\Delta_{y,B}$ $= 253$ mm	$\Delta_{\mathrm{C,E2}} = \Delta_{\mathrm{E2}} - u\Delta_{y,C}$ $= 304$ mm
	Damping of isolator (E1)	$\xi_{IS,A} = 0.250$	$\xi_{IS,B} = 0.250$	$\xi_{IS,C} = 0.250$
	Damping of pier- isolator	$\xi_{eq,A} = 0.250$	$\xi_{eq,B} = 0.209$	$\xi_{eq,C} = 0.226$
	Damping of SDOF system (E1)		$\xi_e = 0.224$	
Step3	Effective period from displacement spectrum		$T_e = 4.62s$	
Step4	Effective period and stiffness (E1)		$K_e = 18.48\ MN/m$	
	Assumed friction coefficient		$\mu = 0.05$	
Step5	Inertial force (E1)	$F_A = 513.25\ kN$	$F_B = 1154.82\ kN$	$F_C = 1283.14\ kN$
	Design stiffness of isolator(E1)	$K_{IS,A} = \frac{\left(\frac{F_A}{2} - F_f\right)}{\Delta_{A,E1}}$ $= 646.50\ kN/m$	$K_{IS,B} = \frac{\left(\frac{F_B}{2} - F_f\right)}{\Delta_{B,E1}}$ $= 1827.58\ kN/m$	$K_{IS,C} = \frac{\left(\frac{F_C}{2} - F_f\right)}{\Delta_{C,E1}}$ $= 1833.58\ kN/m$
	Stiffness of pier(E1)	-	$K_{B,P} = 21459.94\ kN/m$	$K_{C,P} = 50868.00\ kN/m$
Step6	Parameters of MVFPI (Eq.(1))	$T_0 = 2.00$ s, $\mu = 0.05$, b = 0.367 m, d = 0.604 m	$T_0 = 2.00$ s, $\mu = 0.05$, b = 0.396 m, d = 0.627 m	$T_0 = 2.00$ s, $\mu = 0.05$, b = 0.376 m, d = 0.611 m
	New damping of isolator (E1)	$\xi'_{IS,A} = 0.235$	$\xi'_{IS,B} = 0.236$	$\xi'_{IS,C} = 0.236$
		E2 hazard level design		
Step2	Damping of isolator w/o SMA(E2)	$\xi_{IS,A} = 0.144$	$\xi_{IS,B} = 0.160$	$\xi_{IS,C} = 0.152$
	Damping of pier-isolator (E2)	$\xi_{eq,A} = 0.144$	$\xi_{eq,B} = 0.180$	$\xi_{eq,C} = 0.162$
	Damping of SDOF system(E2)		$\xi_e = 0.145$	
Step3	Effective period from displacement spectrum		$T_e = 3.90\ s$	
Step4	Effective period and stiffness (E2)		$K_e = 25.93\ MN/m$	
Step5	Design stiffness of isolator (E2)	$K_A = 1187.18\ kN/m$	$K_B = 3966.06\ kN/m$	$K_C = 3662.44\ kN/m$
	Stiffness of isolator w/o SMA (E2)	$K_{\mathrm{A,E2}} = 865.27k\ N/m$	$K_{B,E2} = 2156.36\ kN/m$	$K_{C,E2} = 2299.60\ kN/m$
Step6	Design force of SMA (E2)	$V_{SMA,A}$ $= (K_A - K_{A,E2}) \times \Delta_{A,E2}$ $= 120.72kN$	$V_{SMA,B}$ $= (K_B - K_{B,E2}) \times \Delta_{B,E2}$ $= 457.07kN$	$V_{SMA,C}$ $= (K_C - K_{C,E2}) \times \Delta_{C,E2}$ $= 414.15kN$
	Damping of IS with SMA (E2)	$\xi'_{IS,A} = 0.151$	$\xi'_{IS,B} = 0.170$	$\xi'_{IS,C} = 0.162$

Appendix II

Table II Selected Ground Motion Records

No.	Earthq. Name	Year	Station Name	Magnitude	R_{rup} (km)	V_{s30} (m/sec)
1	Imperial Valley	1940	El Centro Array #9	6.95	6.09	213.44
2	Borrego	1942	El Centro Array #9	6.50	56.88	213.44
3	Kern County	1952	LA - Hollywood Stor FF	7.36	117.75	316.46
4	Kern County	1952	Taft Lincoln School	7.36	38.89	385.43
5	Northern Calif-03	1954	Ferndale City Hall	6.50	27.02	219.31
6	El Alamo	1956	El Centro Array #9	6.80	121.70	213.44
7	Hollister-01	1961	Hollister City Hall	5.60	19.56	198.77
8	Parkfield	1966	Shandon Array #12	6.19	17.64	408.93
9	Parkfield	1966	Shandon Array #5	6.19	9.58	289.56
10	Parkfield	1966	Shandon Array #8	6.19	12.90	256.82
11	Borrego Mtn	1968	El Centro Array #9	6.63	45.66	213.44
12	San Fernando	1971	2516 Via Tejon PV	6.61	55.20	280.56
13	San Fernando	1971	Carbon Canyon Dam	6.61	61.79	235.00
14	San Fernando	1971	Fairmont Dam	6.61	30.19	634.33
15	San Fernando	1971	LA - Hollywood Stor FF	6.61	22.77	316.46
16	San Fernando	1971	Port Hueneme	6.61	68.84	248.98
17	San Fernando	1971	Puddingstone Dam	6.61	52.64	421.44
18	San Fernando	1971	Santa Felita Dam (Outlet)	6.61	24.87	389.00
19	San Fernando	1971	Whittier Narrows Dam	6.61	39.45	298.68
20	Managua	1972	Managua_ ESSO	5.20	4.98	288.77
21	Saguenay	1988	US.ISFL	5.85	320.51	866.70
22	AuSableForks	2002	St-Roch-des-Aulnaies_ QC	4.99	405.14	2000.00
23	AuSableForks	2002	Riviere-Ouelle_ QC	4.99	433.53	2000.00
24	AuSableForks	2002	St-Simeon_ QC	4.99	468.92	2000.00
25	ValDesBois	2010	Bathurst_ NB	5.10	735.28	2000.00
26	ValDesBois	2010	McAlpine Lake_ ON	5.10	555.89	2000.00
27	ValDesBois	2010	Baie Johan Beetz_ QC	5.10	1057.50	2000.00
28	ValDesBois	2010	Victor Mine_ ON	5.10	970.42	2000.00
29	Greentown	2010	Alfred_ ON	3.85	1063.28	2000.00
30	Greentown	2010	Plevna_ ON	3.85	882.66	2000.00
31	Mineral	2011	Adirondack Community College	5.74	704.24	1250.70
32	Mineral	2011	Allegheny College	5.74	451.34	1014.90
33	Mineral	2011	Brushton-Moira_ NY	5.74	818.25	862.60
34	Mineral	2011	Basking Ridge_ NJ	5.74	420.84	511.50
35	Mineral	2011	Black Rock Forest	5.74	511.85	1185.10
36	Mineral	2011	Flat Rock_ Altona_ NY	5.74	847.67	1200.60
37	Mineral	2011	Keystone College	5.74	442.73	689.90
38	Mineral	2011	Middlebury College_ Vermont	5.74	786.91	1473.90
39	Mineral	2011	Newcomb_ NY	5.74	739.45	1197.40
40	Mineral	2011	Mohonk Preserve	5.74	533.62	1500.00

Table II Continued

No.	Earthq. Name	Year	Station Name	Magnitude	R_{rup} (km)	V_{s30} (m/sec)
41	Mineral	2011	Palisades_ NY	5.74	485.48	1064.60
42	Mineral	2011	SUNY Potsdam_ NY	5.74	786.88	555.00
43	Mineral	2011	West Valley_ NY	5.74	498.32	1798.90
44	Mineral	2011	NP.2549	5.74	249.71	1050.30
45	Mineral	2011	Bancroft_ ON	5.74	785.93	2000.00
46	Mineral	2011	Walkerton_ ON	5.74	735.26	500.00
47	Mineral	2011	Deloro Mine_ ON	5.74	730.68	2000.00
48	Mineral	2011	Darlington East_ ON	5.74	661.28	2000.00
49	Mineral	2011	Medina	5.74	581.15	500.00
50	Mineral	2011	Prince Edward County_ ON	5.74	670.19	1700.00
51	Mineral	2011	Pelee Island	5.74	580.22	2000.00
52	Mineral	2011	Tyneside_ ON	5.74	594.11	404.00
53	Mineral	2011	Wesleyville_ ON	5.74	665.04	1137.00
54	Mineral	2011	Palisades_ NY	3.97	482.68	1064.60
55	Sparks	2011	Lake Charles_ LA	4.73	502.49	564.30
56	Sparks	2011	Wooly Hollow	4.73	400.28	1403.00
57	Sparks	2011	White Oak Lake	4.73	388.64	556.10
58	Sparks	2011	French Village_ MO	4.73	619.10	635.30
59	Sparks	2011	Olney Central College Olney	4.73	838.65	475.00
60	Sparks	2011	St. Louis_ MO	4.73	666.37	312.00
61	Sparks	2011	University of Arkansas	4.73	405.11	1288.00
62	Sparks	2011	Smith Ranch_ Marlow	4.73	148.55	548.40
63	Sparks	2011	Ozark Folk Center	5.68	417.95	592.90
64	Sparks	2011	Wilshire Boulevard; Harrah	5.68	39.73	725.00
65	Sparks	2011	Cathedral Cave	5.68	563.83	463.80